Autonomous Optical Survey Based on Unsupervised Segmentation of Acoustic Backscatter

Øystein Sture, Trygve Olav Fossum, Martin Ludvigsen
Norwegian University of
Science and Technology (NTNU),
& Centre of Autonomous Marine Operations and Systems (AMOS)
Department of Marine Technology,
7491 Trondheim, Norway

Martin Syre Wiig
Norwegian Defence Research
Establishment (FFI)/NTNU,
P.O. Box 25, N-2027 Kjeller, Norway

***Abstract*—The application of acoustics to study the seabed have for decades provided industry and science with valuable information, and is still excels in terms of spatial coverage and detail. An acoustic response from the seabed not only contains information about the range, through the two way travel time, but also the acoustic reflectivity of the substrate from the strength of the backscatter response. As the signal strength differs between substrate types, this information can be used to detect and classify different seabed types. However, there are ambiguities in the acoustic signatures and the reliance on ground truth samples, for succeeding in this identification, is a limiting factor. In this paper we present a way to mitigate this problem using Hidden Markov Random Fields (HMRF) to perform unsupervised segmentation of the backscatter response for the purpose of determining different seabed types. The outcome of this analysis is directly used to plan and conduct an autonomous near-seabed camera survey to verify the classification results, whilst complementing the acoustical data-set. The method is tested in a full-scale experiment and performed in-situ onboard a Kongsberg Hugin 1000 autonomous underwater vehicle (AUV).**

I. Introduction

The deep seas are increasingly being explored in search of natural resources and to promote scientific understanding of deep-sea ecosystems and seafloor processes. Bathymetry and backscatter measurements from acoustics has been used as tools to map hydrocarbon seeps [1], hydrothermal seafloor vent sites [2], polymetallic nodule fields [3], the presence of active volcanic processes [4], cold seep fauna and habitats [5]. Shared for deep sea exploration is the relatively large areas that has to be covered and time consuming launch and recovery for near-seabed surveying. The use of autonomous underwater vehicles (AUVs) can facilitate adaptive patterns in response to the collected data, thus potentially enhancing the collected data during the same deployment.

Supervised learning methods have previously been used for segmenting the seabed into sets of known classes such as gravel, sand, silt and mud [6]. A ground truth in the form of labeled samples or images is however required prior to training. This typically involves deployment of a remotely operated vehicle (ROV), to obtain physical sediment samples or video verification. Samples are also necessary for traditional or manual seabed classification, where seabed features are defined locally and extrapolated using backscatter data. Variations in regional seabed characteristics, equipment, calibration and environmental factors can prohibit transferring trained classifiers or verification data to new areas.

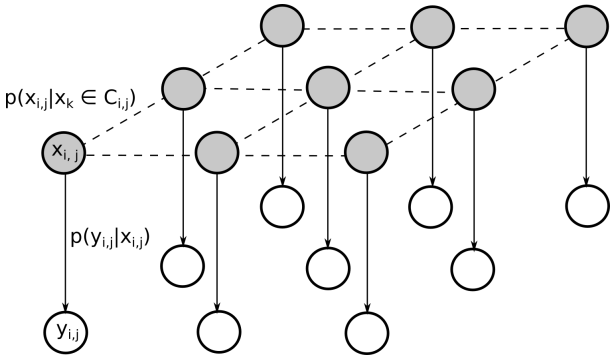

Fig. 1. Illustration of a hidden Markov random field in two dimensions with an iid. observation model. The hidden layer is depicted in gray and observations in white.

Furthermore, there is variability in the equipment itself. Multi-beam echosounders typically transmit using a single centre frequency at a time. Many have several settings for the centre frequency, which provides a trade-off between the resolution and range. The backscatter response is generally dependent on the selected frequency and pulse length. It therefore has some inherent ambiguity, as different scattering mechanisms can yield near identical responses over a range of grazing angles for different material types. Multi-frequency acoustic systems, gathering backscatter data across multiple frequencies simultaneously, has been suggested as a way to mitigate this ambiguity [7]. Another effect that adds to the inherent ambiguity of backscatter is the presence of organized roughness of the seabed. This can for example be ripples in sandy sediments, caused by tidal currents. The acoustic backscatter can then differ based on the survey azimuth, even from signals in the same area [8].

The ambiguity in backscatter data can be minimized through robust calibration routines, but is still difficult to apply without verification data. Gathering multi-beam data from an AUV allows for near-seabed camera lines planned in-situ, which

reduces the need for additional sampling after the first deployment. In this paper, results from an unsupervised near-seabed survey experiment – performed autonomously – is presented.

The remainder of this paper is organized as follows: Section II presents hidden Markov models and how it is used in the context of seabed mapping. Section III presents the pre-processing of the acoustic backscatter prior to segmentation. Section IV briefly describes the AUV and practicalities surrounding the experiment. Section V describes the experiment, segmentation and the path planning. Section VI briefly describes the optical results. Finally, the paper is concluded with a general discussion surrounding the results and future work in section VII.

II. Hidden Markov Random Fields

Hidden Markov Models (HMMs) are stochastic models where the process is composed of states, which cannot be observed directly. The probability distribution of a hidden state is dependent on the value of the states preceding it. In the HMM model this can be thought of as a chain of states, where the dependency between them can for example be in space or time. To make the problem tractable for large problems with a high number of hidden states, the history of the process is assumed to be encoded fully into a limited number of past states (referred to as *the Markov property*). A Hidden Markov Random Field (HMRF) is a generalization of the hidden layer to multiple dimensions, where the probability distribution is conditional on a set of co-variates, e.g. the spatial neighbourhood. In this work, the hidden states are taken to be discrete, or categorical, where one state is attributed to a certain seabed class. Figure 1 contains an concept illustration of an HMRF defined on a square lattice with an identical and independently distributed (iid) likelihood model, i.e. observation model.

Let $\mathcal{L} = \{1, 2, \ldots, L\}$ be the set of possible values for the hidden states, where categorical labels are represented as integers. The hidden layer is given by the states

$$\mathcal{X} = \{x_i, \ldots, x_n | x_i \in \mathcal{L}\}$$

These hidden nodes forms an undirected graph $\mathcal{G} = \{\mathcal{V}, \mathcal{E}\}$, where the vertices $\mathcal{V}$ are the hidden states and $\mathcal{E}$ are the edges that connect them. The neighbourhood set $\mathcal{C}_i$ of a node consists of the nodes that are directly connected to it.

$$\mathcal{C}_i = \{j \in \mathcal{V} | (i, j) \in \mathcal{E}\}$$

Given its neighbourhood set, a node is independent of the rest of the nodes in the graph due to the Markov property. That is, its conditional probability is fully determined by by $P(X_i | X_j \in \mathcal{C}_i)$. This is important, as global labeling can be performed by considering local properties.

For regular HMMs, dynamical programming principles can be used to compute the *posterior marginal distributions* of the hidden states given the observations, $P(X_k | y_{1:n})$, and the most likely sequence of states. However, these algorithms does not directly apply to inference with general graphs that contains loops. In these instances one must typically use approximations or Markov Chain Monte Carlo (MCMC) techniques and accept a trade-off between accuracy and computational burden.

Maximum a posteriori (MAP) estimation seeks to find the most probable value for a random variable given its likelihood function and prior probability. We take the prior probability to be given by the configuration of the HMRF. The criterion we seek to maximize can be stated as follows

$$\hat{\mathbf{x}} = \arg\max_{\mathbf{x}} \{P(\mathbf{y}|\mathbf{x}, \mathbf{\Theta}_L) P(\mathbf{x})\} \tag{1}$$

That is, we are interested in finding the mode of the posteriori distribution given a likelihood function of known parameters Θ_L and the observation. In this work the likelihood function is taken to be a Gaussian distribution with unknown parameters, (μ_L, σ_L) that must be estimated for each label L.

$$P(\mathbf{y}|\mathbf{x}, \mathbf{\Theta}_L) \sim \mathcal{N}(\mu_L, \sigma_L)$$

The HMRF prior model, $P(\mathbf{x})$, can be represented in terms of local energies or cost functions defined on each neighbourhood (maximal cliques). The equivalence of the local properties and global properties has been established in the Hammersley-Clifford theorem [9]. The local energy function can be defined as

$$P(\mathbf{x}) = \frac{1}{Z} e^{-U(\mathbf{x})} \tag{2}$$

Where

$$U(\mathbf{x}) = \sum_{c \in \mathcal{C}} \Psi_c(\mathbf{x}), \quad Z = \sum_{x \in \mathcal{X}} e^{-U(x)}$$

is the sum of clique potentials, or local energies $\Psi_c(\mathbf{x})$, and a normalizing constant Z (also called the partition function). The clique potential function selected depending on the problem to exhibit the desired global characteristics. For this experiment, the *Potts model* was selected as the prior energy function, which penalizes any non-zero difference between labels equally regardless of which labels are compared [10].

$$\Psi(x_i, x_j) = \lambda \min\{(x_i - x_j)^2, 1\} \tag{3}$$

The parameter, λ, adjusts the strength of the smoothness prior. A value of $\lambda = \frac{1}{3}$ was used with a 5x5 neighborhood.

To calculate the exact prior distribution, Z must be evaluated, which involves a sum over all possible configurations in $\mathcal{X}$. This is prohibitive even for problems of moderate size [11]. The same approach as [12] is therefore taken, where the problem is solved using a greedy strategy through iterative optimization (iterated conditional modes). This approach converges fast, but has no global optimal guarantees and can be sensitive to the choice of initial values.

The unknown parameters (μ_L, σ_L) of the likelihood function are estimated through expectation maximization (EM) given a fixed configuration for the Markov field. First, the posterior distribution is computed using Bayes rule.

$$P(L|y_i) = \frac{p(y_i|x_i, \theta_L, \sigma_L)p(L|x_i, \mathcal{C}_i)}{p(y_i)} \tag{4}$$

Where y_i are the observations and L are the possible hidden states. The parameters are then updated as

$$\mu_L^+ = \frac{\sum_{i=1}^n P(L|y_i)y_i}{\sum_{i=1}^n P(L|y_i)} \tag{5}$$

$$\sigma_L^+ = \frac{\sum_{i=1}^n P(L|y_i)(y_i - \mu_L)^2}{\sum_{i=1}^n P(L|y_i)} \tag{6}$$

In practice, the combined estimation of labels and likelihood function parameters is done through alternating steps of expectation maximization (EM) and maximum a posterior prediction (MAP). EM updates the mean and variance for each class given a fixed spatial configuration, whereas MAP updates the spatial configuration (labeling) given a fixed likelihood model for each class. To get the process of iterative MAP and EM stages started, the initial likelihood parameters are estimated based on a K-means clustering of the observations.

III. Multibeam Backscatter

The physical process of seafloor scattering can be considered to be a random process [13]. The envelope of narrow-beam acoustic reverberation has a tendency to follow a log-normal distribution at low grazing angles, especially for a moving observer [14]. When including the near-*nadir* region the distribution becomes skewed and is better characterized as a log-gamma distribution [15].

For the purpose of segmentation, it is desirable to have a normalized mean across the swath. In particular, the physical backscattering process has a dependency on the grazing angle, which varies with the seabed type. This causes the backscatter to deviate systematically across the swath. By removing the angular dependency through normalization, the full swath can be used uniformly for segmentation. For seabed classification on the other hand, this variation with angle is desirable as it provides additional information about the seabed substrate.

The multi-beam used in this experiment was the Kongsberg EM2040. It has built-in compensation for frequency-dependent transmission loss, spherical spreading, ensonification area, and angular seabed response variation. These corrections are applied based on the assumption of a flat seabed and a fixed angular response model [16]. The system stores the necessary values to remove these corrections. These values were not available through the Hugin SDK backseat control system (used to control and interface with the sensors and AUV) at the time of the experiment, and the removal of these assumptions during online processing is therefore left to future work. Due to the imperfect normalization, a component which depends on incidence angle remains. This is the component that the normalization steps will seek to remove. The approach is similar to what would be done had the aforementioned assumptions been corrected for, but may contain artifacts from the built-in correction routine.

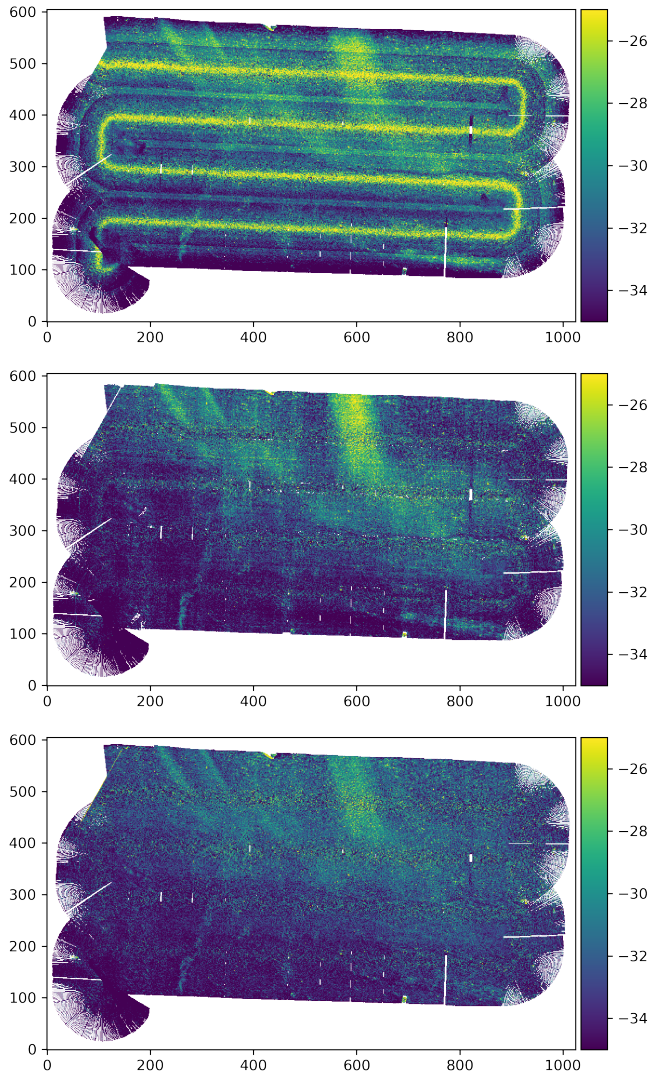

Fig. 2. Comparison of the backscatter output directly from EM2040, sliding-window normalization, and Kalman filtered backscatter respectively. The units of the axes are in meters, and the color-scale in dB.

The subsequent procedure is conceptually similar to the angular dependence correction outlined in [13]. In this procedure, the responses are placed into angular bins based on the incidence angle, where each bin is 1° wide. The mean level of each bin is computed for a subset of the data. The difference between these averaged values and a reference level is then added as a normalization factor. The reference values are typically an per-ping average across some portion of the swath, excluding the specular returns around nadir. The averaging is either performed for a whole survey line at a time or based on a *sliding window*. A large window better compensates for statistical variation, but increases the chance of averaging over multiple seabed types with different angular responses. This may cause a problem as the average over the incidence angle bins will contain not one, but multiple signatures.

Rather than using a sliding window approach, we tackle the problem by considering the per-angle bias to be a *Wiener*

process, i.e. a random walk process. The normalization values are considered biases that must be estimated. This is done by applying a *Kalman filter* per incidence angle. Note that this makes an assumption of a normally distributed noise process, which has been pointed out is not the case for the near-nadir region. Consequently, we accept that there will be a bias in the estimate in this region, and leave an optimal estimator to future work. The Gaussian assumption allows for better computational characteristics on the other hand, as there is no closed-form solution for the mode of a gamma distribution. The filter is a simple integrated noise process, formulated as follows in continuous time.

$$\begin{aligned} \dot{x}_\phi &= w \\ y_\phi &= x_\phi + v \end{aligned} \tag{7}$$

Where the incidence angle bin is indicated by the angle ϕ, w is the process noise driving the random walk process, and v is the measurement noise. The measurement presented to the filter is the difference between the measured backscatter for that incidence angle and the mean backscatter measurement $z_\theta = a_\phi - \bar{a}$. The mean across the swath starts from $\theta = \pm 15$ to avoid the specular returns around the nadir region.

Instead of adjusting the length of the sliding window, the co-variance of the random walk process and noise process are tuned. The process co-variance is set according to how quickly the underlying seabed substrate changes its characteristics, while the noise co-variance is set according to the expected noise in the measurements themselves. The interested reader is referred to [17] for the Kalman update equations and underlying theory. Both of these parameters are likely to vary in their applicability based on the region being surveyed and survey pattern. This is also the case for the length of the window in the sliding window approaches however.

The collected backscatter was normalized for each ping and then interpolated to a fixed grid, weighted by its quality factor. The quality factor is the standard deviation of the measured time-series weighted by the range [18], and is one of the outputs from the system. A comparison of the raw output from the echosounder and re-normalized backscatter can be seen in Figure 2.

The built-in normalization has some clearly visible artifacts. Notably, there is a crossover artifact around half the width of the swath, where it switches between two models of angular variation. It is also unable to normalize the region around nadir properly. The middle figure contains a re-normalization of the EM2040 output using a sliding window average approach with a window size of 400 pings. Finally, a normalization based on bias estimation using Kalman filters is shown. A quantitative comparison of the normalization schemes is not performed here, as this should be performed on raw data without the Kongsberg time-varying gain and normalization applied. The Kalman filtered approach seems to provide a slightly smoother nadir area, which helps during the segmentation.

IV. Equipment

The AUV used for this expedition was the Kongsberg Hugin 1000 HUS. Overall specifications is shown in Table I. Hugin is equipped with a dedicated payload processor, where plugins can be loaded to perform remote/backseat control tasks. Its processing time is however shared with other functions such as data logging and sensor control. Autonomy on AUVs can require interpretation of spatial and/or temporal data, which can be computationally intensive. This can interfere with the other running tasks on the payload processor, or not receive high enough priority to perform the autonomy tasks successfully. As a solution to this problem a co-processor dedicated to autonomy was used, allowing algorithms to be designed and tuned with a fixed processing power in mind. A Nvidia Jetson TX2 was used as this stand-alone co-processor.

TABLE I
Kongsberg Hugin 1000 HUS specifications

Weight	$\sim$1000 kg
Length	$\sim$5.5 m
Diameter	$\sim$0.75 m
Speed	1.0 m s^{-1} to 3.0 m s^{-1}
Depth	3000 m
Endurance	16hrs @ 2.1 m s^{-1}, with instruments
Navigation	INS: IMU, DVL, depth, USBL, GPS, Compass, Terrain navigation, UTP
Communication	Acoustic, RF, Iridium, Ethernet, WLAN
Ex. payloads	EM2040 MBE, HISAS 1030 SSS, CTD, ADCP, Camera, Chemical sniffer, Sub-bottom profiler

The software integration consisted of a backseat plugin running on the payload processor, which interfaces with the AUV through the Hugin software development kit (SDK). This plugin acts as a translation layer between the Nvidia Jetson TX2 and Hugin for sensor data and remote control commands. The message protocol defined in the LSTS toolchain (IMC) was used for the data exchange [19]. More details of the integration can be found in the cruise report from the experiment [20].

V. Experiment

The following section presents the experiment that was performed and the steps performed on the normalized backscatter once the whole area had been covered. The survey area was selected based on side-scan sonar data from 2013, shown in Figure 3, where a boundary between two types of sediments was clearly visible, possibly due to a subsurface landslide.

The experiment was executed by first covering a target area in a pre-planned survey. Upon completion, the autonomous survey was initiated through a command over the acoustic communications link. The takeover could easily be done automatically, but was left semi-automatic to retain as much control as possible during the experiment.

A. Segmentation

Following coverage of the area, the backscatter is segmented into a discrete number of classes by modeling the probability distribution as a hidden Markov random field (HMRF) with

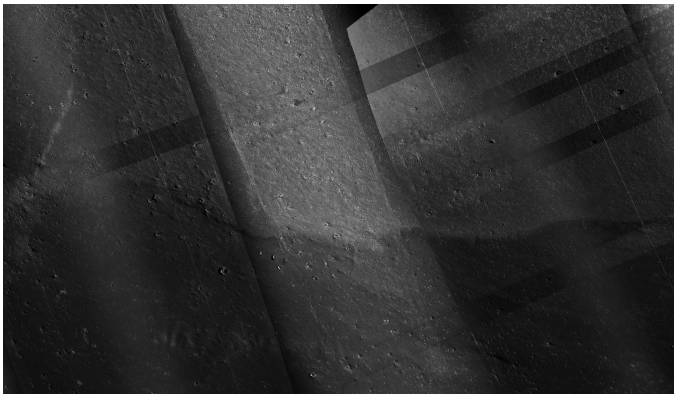

Fig. 3. Synthetic aperture sonar previously gathered in the target area. This was used to pick the location for the experiment.

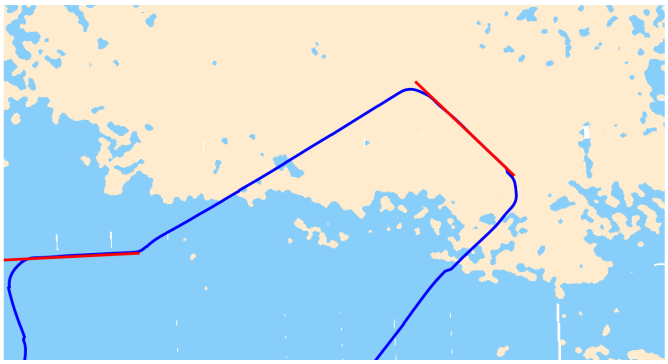

Fig. 4. Segmentation of the normalized backscatter into two classes, with the generated camera lines in red and actual path of the AUV in blue.

a Gaussian likelihood model. This model accounts for seabed types being characterized by distinct Gaussian distributions, but also integrates the notion that a location is more likely to belong to the same class as its neighbors. The result can be seen in Figure 4. The relatively square edges along the survey directions are possibly artifacts from the time-varying gain applied by the instrument as it crosses the areas.

If an additional class is added to the segmentation, the small area at the top is separated into its own class, but the nadir area also has a visible impact on the result.

B. Path Planning

One camera transect per class was planned by maximizing the distance to other classes, and joined together by minimizing the distance traveled. To represent distance to other classes, the distance transformation is applied to the segmented image [21]. The transformation is applied once per class, where all other classes are considered to be a boundary. The portions with missing data are not considered to be boundary objects if in the interior of the class being considered. This in practise causes the distance transform to ignore small interior holes, but also assumes that the area has sufficient coverage. The distance transform performed on the segmented backscatter is shown in Figure 5.

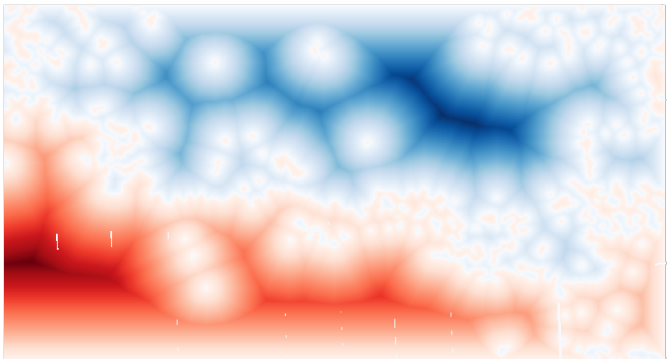

Fig. 5. Distance transform for the two classes being considered.

An heuristic approach to the path planning was chosen, where local maxima of the distance transform is used as the center-point for the camera lines. A discrete number of orientations of the camera lines are evaluated by taking the sum over the distance transform along each orientation. The orientation with the highest value was selected for this experiment, but one could also imagine this to be embedded into an optimization problem which weighs the distance traveled against the separation between the classes. The camera lines are connected by casting the problem into a traveling-salesman formulation, where the center of the camera line is a location that must be visited, only accessible through its entry and exit line. Since the number of classes were low in this experiment, this was solved by brute force, but approximation strategies can be applied for the problem in the general case.

For general path planning, a soft threshold should be applied to the distance transform to upper bound the reward by moving away from the other class. This is especially important when weighting the distance travelled against the class separation. A sigmoidal function can for example be utilized for this purpose.

VI. Results

The experiment was performed in a fjord with relatively high turbidity, and hence the visibility of the seabed from the AUV was low. Both a conventional camera and underwater hyperspectral imager (UHI) was mounted on the AUV. The RGB camera was not able to observe the seabed, however. For this reason the UHI is used. The altitude set-point of the camera lines were set at $6\,\mathrm{m}$ due to operational constraints such as collision avoidance requirements, pitch capability, and the likelihood of encountering seabed rockfaces. An RGB projection of the hyperspectral imagery can be seen in Figure 6.

The noise level of the images are apparent, and are inconclusive with respect to the texture of the seabed. There is a slight shift in brightness for the second camera line compared to the first however. This is also observed in Figure 7, where an averaged spectral response for the transects are shown. The average is taken at the middle of the cross-section, to avoid issues with varying attenuation with distance.

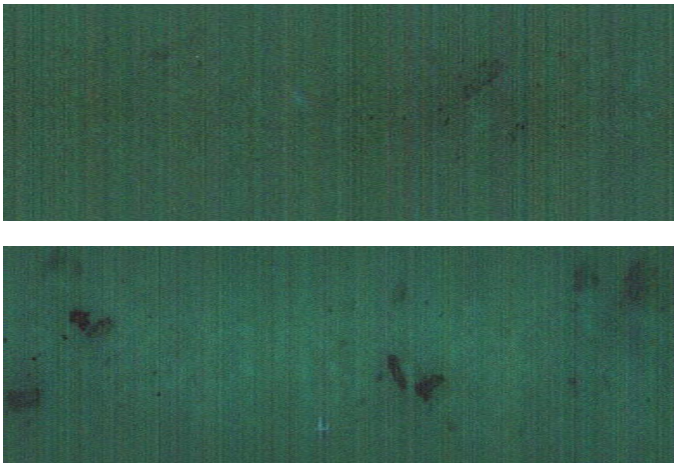

Fig. 6. Excerpt from camera line 1 and 2 respectively. These images are RGB projections from the hyperspectral underwater imager (UHI), which has highly light sensitive optics. The images are normalized for cross-track variability using the same normalization values for both camera lines.

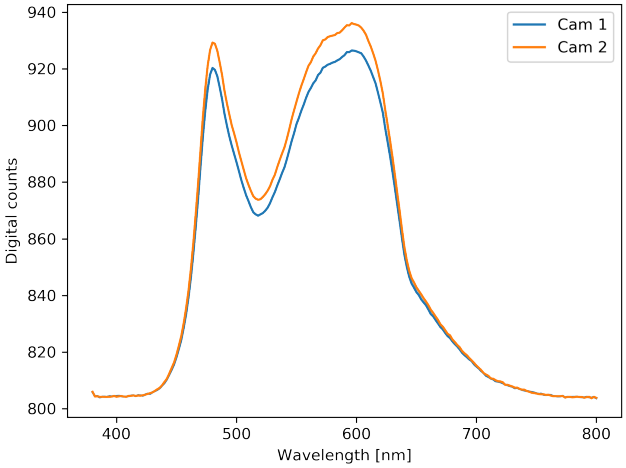

Fig. 7. The raw digital counts of the hyperspectral camera obtained by taking the mean along the middle part of the swath for each camera line. These values has not been normalized in any way, and the altitude was fairly constant at 5.8 m to 6.0 m .

The possibility that the turbidity in the water changed slightly from one camera line to the next cannot be excluded however.

VII. Discussion

An autonomous near-seabed survey was performed by segmenting the acoustic backscatter response and visiting each class by maximizing the distance between the camera lines and the class boundary. Figure 8 contains plots of the probability density functions of the estimated backscatter classes. The histogram is a collection of all values. Due to the central limit theorem, it is expected that the collection of all the seabed responses will tend towards a normal distribution. This illustrates that it is difficult to segment the seabed without considering the spatial localities.

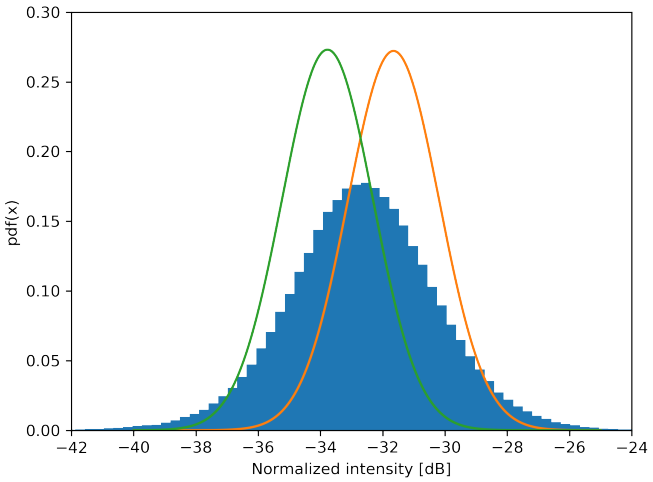

Fig. 8. The two classes found are given by $\mu_L = \{-31.5, -33.8\}$ and $\sigma_L = \{1.47, 1.45\}$. The probability density functions of these are shown together with a normalized histogram of all soundings combined.

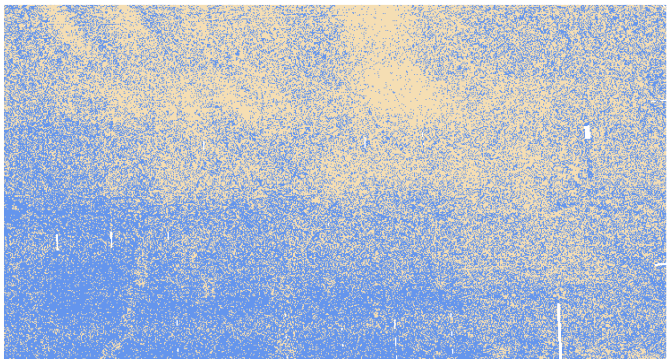

Fig. 9. The segmented map according to the likelihood models estimated, applied without any spatial smoothing.

Figure 9 shows the case where Bayes classification is performed using the two found distributions. This illustrates the amount of spatial smoothing that is applied by the prior model.

While the approach worked well for this small-scale experiment, there are unresolved issues that must be addressed before the method can be applied in the general case.

First, the path planning described here does not take the bathymetry into account in its planning. While this problem can be mitigated by excluding problematic areas, the general case can be solved through discrete or continuous optimization by including a penalty in the cost function.

Second, the selection of the number of classes has not been discussed. For this experiment, the area was of limited extent, and the expected number of classes was known and fixed ahead of time. The problem of determining the number of classes can either be approached heuristically by considering the morphology of the segmented areas, or statistically by considering the estimated likelihood parameters for a given number of classes. The closeness of the distributions can be quantified through information theoretic metrics such as the

Kullback-Leibler divergence or Bhattacharyya distance [22], [23]. Alternatively, one can consider the parameter space a part of the inference problem. This be estimated through non-parametric Bayesian inference, using MCMC or variational inference methods [24]–[26]. The computational cost for these methods can be prohibitive for in-situ usage however.

ACKNOWLEDGMENT

The AUV used was the Kongsberg Hugin 1000 HUS, operated by the Norwegian Defence Research Establishment (FFI). This work was partially funded through Norwegian Research Council grant no. 247626. The LSTS toolchain [19] is available at http://lsts.pt/toolchain.

REFERENCES

[1] G. A. Mitchell, D. L. Orange, J. J. Gharib, and P. Kennedy, "Improved detection and mapping of deepwater hydrocarbon seeps: optimizing multibeam echosounder seafloor backscatter acquisition and processing techniques," *Marine Geophysical Research*, pp. 1–25, 2018.

[2] J. Escartin, T. Barreyre, M. Cannat, R. Garcia, N. Gracias, A. Deschamps, A. Salocchi, P.-M. Sarradin, and V. Ballu, "Hydrothermal activity along the slow-spreading lucky strike ridge segment (mid-atlantic ridge): Distribution, heatflux, and geological controls," *Earth and Planetary Science Letters*, vol. 431, pp. 173–185, 2015.

[3] C. Rühlemann, T. Kuhn, M. Wiedicke, S. Kasten, K. Mewes, A. Picard, *et al.*, "Current status of manganese nodule exploration in the german license area," in *Ninth ISOPE Ocean Mining Symposium*, International Society of Offshore and Polar Engineers, 2011.

[4] D. K. Smith, J. Escartín, H. Schouten, and J. R. Cann, "Fault rotation and core complex formation: Significant processes in seafloor formation at slow-spreading mid-ocean ridges (mid-atlantic ridge, 13–15 n)," *Geochemistry, Geophysics, Geosystems*, vol. 9, no. 3, 2008.

[5] A. Sen, H. Ondréas, A. Gaillot, Y. Marcon, J.-M. Augustin, and K. Olu, "The use of multibeam backscatter and bathymetry as a means of identifying faunal assemblages in a deep-sea cold seep," *Deep Sea Research Part I: Oceanographic Research Papers*, vol. 110, pp. 33–49, 2016.

[6] M. Pierdomenico, V. G. Guida, L. Macelloni, F. L. Chiocci, P. A. Rona, M. I. Scranton, V. Asper, and A. Diercks, "Sedimentary facies, geomorphic features and habitat distribution at the hudson canyon head from auv multibeam data," *Deep Sea Research Part II: Topical Studies in Oceanography*, vol. 121, pp. 112–125, 2015.

[7] J. Hughes Clarke, "Multispectral acoustic backscatter from multibeam, improved classification potential," pp. 15–19, 2015.

[8] X. Lurton, D. Eleftherakis, and J.-M. Augustin, "Analysis of seafloor backscatter strength dependence on the survey azimuth using multibeam echosounder data," *Marine Geophysical Research*, pp. 1–21, 2017.

[9] P. Clifford, "Markov random fields in statistics," *Disorder in physical systems: A volume in honour of John M. Hammersley*, vol. 19, 1990.

[10] A. Blake, P. Kohli, and C. Rother, *Markov random fields for vision and image processing*. Mit Press, 2011.

[11] S. Z. Li, *Markov random field modeling in image analysis*. Springer Science & Business Media, 2009.

[12] Y. Zhang, M. Brady, and S. Smith, "Segmentation of brain mr images through a hidden markov random field model and the expectation-maximization algorithm," *IEEE transactions on medical imaging*, vol. 20, no. 1, pp. 45–57, 2001.

[13] X. Lurton, G. Lamarche, C. Brown, V. Lucieer, G. Rice, A. Schimel, and T. Weber, "Backscatter measurements by seafloor-mapping sonars: guidelines and recommendations," *A collective report by members of the GeoHab Backscatter Working Group*, no. May, pp. 1–200, 2015.

[14] N. Chotiros, H. Boehme, T. Goldsberry, S. Pitt, R. Lamb, A. Garcia, and R. Altenburg, "Acoustic backscattering at low grazing angles from the ocean bottom. part ii. statistical characteristics of bottom backscatter at a shallow water site," *The Journal of the Acoustical Society of America*, vol. 77, no. 3, pp. 975–982, 1985.

[15] I. M. Parnum, *Benthic habitat mapping using multibeam sonar systems*. PhD thesis, Curtin University, 2007.

[16] E. Hammerstad, "Backscattering and seabed image reflectivity," *EM Technical Note*, 2000.

[17] R. G. Brown and P. Y. Hwang, "Introduction to random signals and applied kalman filtering: with matlab exercises and solutions," *Introduction to random signals and applied Kalman filtering: with MATLAB exercises and solutions, by Brown, Robert Grover.; Hwang, Patrick YC New York: Wiley, c1997.*, 1997.

[18] E. Kongsberg, "Series multibeam echo sounders datagram formats," 2015.

[19] J. Pinto, P. S. Diasand, R. Martins, J. Fortuna, E. Marques, and J. Sousa, "The LSTS toolchain for networked vehicle systems," in *MTS/IEEE Oceans*, pp. 1–9, IEEE, 2013.

[20] Ø. Sture, M. Syre Wiig, and T. O. Fossum, "Ntnu-ffi cruise 2017-hugin autonomy integration (dune, t-rex)," *NTNU Cruise reports*, 2017.

[21] G. Bradski, "The OpenCV Library," *Dr. Dobb's Journal of Software Tools*, 2000.

[22] C. Hennig, "Methods for merging gaussian mixture components," *Advances in data analysis and classification*, vol. 4, no. 1, pp. 3–34, 2010.

[23] J. R. Hershey and P. A. Olsen, "Variational bhattacharyya divergence for hidden markov models," in *Acoustics, Speech and Signal Processing, 2008. ICASSP 2008. IEEE International Conference on*, pp. 4557–4560, IEEE, 2008.

[24] P. Orbanz and Y. W. Teh, "Bayesian nonparametric models," in *Encyclopedia of Machine Learning*, pp. 81–89, Springer, 2011.

[25] M. J. Beal, Z. Ghahramani, and C. E. Rasmussen, "The infinite hidden markov model," in *Advances in neural information processing systems*, pp. 577–584, 2002.

[26] H. Attias, "A variational baysian framework for graphical models," in *Advances in neural information processing systems*, pp. 209–215, 2000.